AGU PUBLICATIONS

Paleoceanography

RESEARCH ARTICLE
10.1002/2015PA002850

Key Points:
- New astrochronologic testing method for deep time strata
- Inverse approach evaluates eccentricity-related amplitude modulation and bundling
- Application to PETM-ETM2 interval and Miocene strata

Supporting Information:
- Figures S1–S6
- Software S1
- Software S2

Correspondence to:
S. R. Meyers,
smeyers@geology.wisc.edu

Citation:
Meyers, S. R. (2015), The evaluation of eccentricity-related amplitude modulation and bundling in paleoclimate data: An inverse approach for astrochronologic testing and time scale optimization, *Paleoceanography*, *30*, doi:10.1002/2015PA002850.

Received 22 JUN 2015
Accepted 19 NOV 2015
Accepted article online 21 NOV 2015

The evaluation of eccentricity-related amplitude modulation and bundling in paleoclimate data: An inverse approach for astrochronologic testing and time scale optimization

Stephen R. Meyers[1]

[1]Department of Geoscience, University of Wisconsin-Madison, Madison, Wisconsin, USA

Abstract Cyclostratigraphic analysis has produced fundamental advancements in our understanding of climate change, paleoceanography, celestial mechanics, geochronology, and chronostratigraphy. Of central importance to this success has been the development of astrochronologic testing methods for the evaluation of astronomical-climate influence on sedimentation. Most pre-Pleistocene astrochronologic testing methods fall into one of two categories: (1) those that test for expected amplitude or frequency modulation imposed by an astronomical signal or (2) those that test for bedding hierarchies (frequency ratios or bundling) that are predicted by the dominant astronomical periods. In this study, a statistical methodology for combining these complementary approaches is developed, which identifies the time scale that simultaneously optimizes eccentricity amplitude modulation of the precession band, and the concentration of power at precession (carrier) and eccentricity (modulator) frequencies. The technique is demonstrated to have high statistical power—it is capable of identifying astronomical cycles when present—under a wide range of conditions, and its application to synthetic models illuminates a range of potential pitfalls that are encountered when more conventional nonoptimization approaches are used. The method is also independent from the interpretation of power spectrum peak significance, resolving previous concerns regarding appropriate confidence level assessment and "multiple testing." As two case studies, the algorithm is applied to Miocene strata of Ocean Drilling Program (ODP) Site 926B, and the Paleocene-Eocene Thermal Maximum-Eocene Thermal Maximum 2 interval at ODP Site 1262. The results verify published cyclostratigraphic interpretations and support the theoretical astronomical solutions. This new astrochronologic testing approach can be used to evaluate cyclostratigraphic records spanning the Phanerozoic and potentially beyond.

1. Introduction

The development of in situ high-resolution astronomical time scales has revolutionized our understanding of climate and oceanographic change, and astrochronology now provides a de facto temporal framework for the evaluation of much of Phanerozoic Earth system history [*Gradstein et al*., 2012]. The validity of such time scales is predicated upon accurate identification and calibration of temporal rhythms in strata; to satisfy this requirement numerous quantitative approaches have been developed to test the astronomical hypothesis. The most direct test is provided by so-called "depth-derived" time scales, which apply radioisotopic ages—sometimes with additional constraints—to calibrate spatial rhythms to temporal periods [e.g., *Hays et al*., 1976; *Huybers and Wunsch*, 2004; *Aswasereelert et al*., 2013]. Advances in radioisotopic geochronology [e.g., *Mattinson*, 2005; *Kuiper et al*., 2008] have dramatically enhanced the accuracy and precision of these astrochronologic testing methods. However, the lack of sufficient material for radioisotopic geochronology, and/or poor bio-chemo-magnetostratigraphic constraints for importing time control, often make depth-derived astrochronologic testing approaches ambiguous.

In addition to depth-derived time scales, a number of theoretical astronomical *signal attributes* are often employed to evaluate astronomical influence on climate and sedimentation. For example, bedding hierarchy relationships (frequency ratios or bundling) are regularly used for astrochronologic testing, such as the 5:2:1 relationship between the ~100 ka eccentricity, ~40 ka obliquity, and ~20 ka precession cycles (*Schwarzacher* [1948], *Hays et al*. [1976], *Meyers and Sageman* [2007], *Malinverno et al*. [2010], and many others). Other astrochronologic testing approaches seek to evaluate amplitude or frequency modulations that are expected for the theoretical precession and obliquity signals [*Herbert*, 1992, 1994; *Shackleton et al*., 1995;

Hinnov and Park, 1998; *Hinnov*, 2000]. In principle, these signal attribute techniques are suitable for the analysis of both anchored and floating astronomical time scales [*Hinnov*, 2013]. However, the potential for circularity in such testing has served as a persistent criticism, particularly when evaluating astronomical signal attributes following tuning to an astronomical target curve [*Neeman*, 1993; *Huybers and Wunsch*, 2004; *Huybers and Aharonson*, 2010]. Nonetheless, "minimal" tuning approaches [*Muller and MacDonald*, 2000] and careful signal processing [*Zeeden et al*., 2015] can provide a safeguard against circularity, when executed appropriately. Additional criticisms of astrochronologic testing methods concern spectral analytic approaches, especially the appropriateness of reported confidence levels for power spectrum peaks, underscoring the potential for erroneous interpretation of noise variance as astronomical signal [*Vaughan et al*., 2011; *Meyers*, 2012].

The statistical challenges posed by quantitative astrochronologic testing are formidable [*Meyers et al*., 2008], considering the essential problem of searching for quasiperiodic *temporal* signals in stratigraphic data for which time is often poorly constrained. Additional challenges arise from (1) the gappy and unstable recording of environmental signals within depositional systems (sedimentation rate changes, hiatus), (2) the problem of deciphering (nonlinear) insolation-climate responses that are immersed in noise, including the variable fidelity of climate proxies, and (3) degradation of the theoretical astronomical solutions with age. Regarding the last issue, beyond 50 Ma the amplitudes and phases of the primary astronomical cycles are unknown; however, the expected periods do provide some constraint [*Berger et al*., 1992; *Laskar et al*., 2004, 2011a, 2011b; *Waltham*, 2015], and the 405 ka "long" eccentricity cycle is predicted to be remarkably stable throughout the Phanerozoic [*Laskar et al*., 2004, 2011a, 2011b]. Given the wide range of data analysis issues noted above, and the generally low statistical power of many commonly used astrochronologic testing methods [*Meyers*, 2012], it is extremely difficult to quantitatively confirm astronomical signals when they are present in paleoclimate data.

The intent of the present study is to propose a new solution to this statistical challenge, by combining multiple astronomical signal attributes to produce a more powerful test of the astronomical hypothesis. Specifically, amplitude modulation and frequency ratio (bundling) attributes are evaluated using a probabilistic linear regression model framework. Designated TimeOpt (for "time scale optimization"), this inverse method identifies the sedimentation rate that simultaneously optimizes eccentricity amplitude modulation of the precession band, and the concentration of power at precession (carrier) and eccentricity (modulator) frequencies. A formal evaluation of the null hypothesis of "no astronomical signal," given the optimal sedimentation rate, is conducted using Monte Carlo simulation.

There are a number of desirable features that are central to the new technique. Foremost, TimeOpt is applicable to the entire Phanerozoic. The technique also avoids the interpretation of power spectrum peak significance [*Vaughan et al*., 2011; *Meyers*, 2012], providing an approach that is complementary to other spectrum confidence level-based methods [*Meyers and Sageman*, 2007; *Malinverno et al*., 2010]. Finally, the reconstructed precession and eccentricity signals generated by TimeOpt can be compared to the theoretical astronomical models [*Laskar et al*., 2004, 2011a, 2011b] to improve the solutions and to evaluate the transfer functions that link climate, depositional environment, and sedimentation [*Meyers et al*., 2008]. The phases and amplitudes of the TimeOpt-reconstructed cycles are not predefined in the analysis, but rather are emergent properties; thus, they provide an objective means for testing of the theoretical astronomical solutions.

The statistical power of TimeOpt is evaluated using a series of synthetic models, which reveal that the method is capable of identifying astronomical cycles (when present) under a wide range of conditions. These numerical experiments also demonstrate how TimeOpt is a useful tool for studying the interplay between noise and astronomical signal, illuminating a number of potential pitfalls that are encountered when frequency ratio and amplitude modulation approaches are implemented in a conventional (nonoptimization) manner. As two example case studies, TimeOpt is used to evaluate cyclic Miocene strata from Ocean Drilling Program (ODP) Site 926B at Ceara Rise [*Pälike et al*., 2006a], and the Paleocene-Eocene Thermal Maximum-Eocene Thermal Maximum 2 (PETM-ETM2) interval at ODP Site 1262 in the Angola Basin [*Lourens et al*., 2005; *Westerhold et al*., 2007]. In both cases, the TimeOpt results confirm published astronomical interpretations with a high degree of statistical significance (at the 99.5% confidence level), and yield time-calibrated astronomical signals that are evaluated against the theoretical eccentricity models. The comparison

Table 1. Eccentricity and Precession Target Periods Used in the TimeOpt Analyses[a]

Site 1262		Site 926B	
Eccentricity (ka)	Precession (ka)	Eccentricity (ka)	Precession (ka)
405.7	23.0	405.7	23.4
130.7	21.8	130.7	22.2
123.8	18.6	123.8	18.8
98.9		98.9	
94.9		94.9	

[a]The eccentricity periods are nominal values estimated via spectral analysis of the *Laskar et al.* [2011a] "10d" solution spanning 0–20 Ma (these periods are identical to those determined using the *Laskar et al.* [2004] solution). In contrast to the eccentricity periods, the precession periods are influenced by changes in Earth's rotation rate and the dynamical ellipticity of the planet; the precession periods were estimated via spectral analysis of the *Laskar et al.* [2004] astronomical solution spanning 53–56 Ma (Site 1262) and 20–23 Ma (Site 926B).

between observed and theoretical eccentricity signals provides new insight into climate response and the validity of the theoretical astronomical solutions.

2. TimeOpt: Time Scale Optimization Through an Evaluation of Eccentricity-Related Amplitude Modulation and Bundling

TimeOpt is an astronomical testing approach for *untuned* stratigraphic data that comprehensively evaluates a range of plausible time scales for deposition. For a given a depth-scaled (meters) climate proxy data series ($\mathbf{y_{data}}$), this inverse method seeks to identify the sedimentation rate that simultaneously optimizes eccentricity-related amplitude modulation of the precession band, and the concentration of spectral power at precession (carrier) and eccentricity (modulator) frequencies. The analysis is conducted in three steps, which independently evaluate the amplitude modulation (or "amplitude envelope") and spectral power, and then combine these results. Statistical significance of the best fit result is determined via Monte Carlo simulation.

For each temporal calibration investigated (sedimentation rate), the observed precession-band amplitude envelope is extracted using band-pass filtering and the Hilbert transform [*Taner et al.*, 1979]. The fit of the extracted precession envelope to the expected eccentricity periods is evaluated using a probabilistic linear regression model (equation (1)), where the optimal model at each sedimentation rate is identified by least squares estimation:

$$\mathbf{y_{envelope}} = \mathbf{X_e}\boldsymbol{\beta}_\mathbf{e} + \boldsymbol{\varepsilon} \quad (1)$$

Where:

$\mathbf{y_{envelope}}$ is the precession-band amplitude envelope for the temporally calibrated data series
$\mathbf{X_e}$ is a matrix of sine and cosine predictor terms representing the eccentricity periods
$\boldsymbol{\beta}_\mathbf{e}$ is a vector of regression coefficients for each predictor
$\boldsymbol{\varepsilon}$ is a vector of error terms

Five dominant eccentricity periods (405.7, 130.7, 123.8, 98.9, and 94.9 ka [*Laskar et al.*, 2011a] Table 1) are used as predictors in equation (1) ($\mathbf{X_e}$). The amplitudes and phases of the eccentricity terms are determined during the linear model optimization; this approach is advantageous because the amplitudes and phases of the main astronomical terms are unconstrained for deep-time investigations (>50 Ma), in contrast to their periods [*Berger et al.*, 1992; *Laskar et al.*, 2004; *Laskar et al.*, 2011b; *Waltham*, 2015]. Furthermore, the transfer functions associated with the climate and depositional system can alter the amplitudes and phases of the theoretical astronomical terms (as in *Hays et al.* [1976], *Laurin et al.* [2005], *Swenson* [2005], and *Meyers et al.* [2008]), a factor that this numerical approach explicitly accommodates.

The probabilistic model of equation (1) is evaluated across a grid of sedimentation rates constrained by radioisotopic and/or bio-chemo-magnetostratigraphic data. The quality of the *fit* at each sedimentation rate is then estimated using the Pearson correlation coefficient (or alternatively Spearman's rank correlation coefficient [*Spearman*, 1904]) between the fitted eccentricity model, $\mathbf{f}(\mathbf{X_e},\boldsymbol{\beta}_\mathbf{e})$, and the observed precession band

envelope ($\mathbf{y_{envelope}}$). The resulting correlation, $r^2_{envelope}$, indicates the fraction of variance shared between the model and temporally calibrated amplitude envelope at a given sedimentation rate.

The concentration of spectral power at the target astronomical periods for each temporal calibration is evaluated using a second probabilistic linear regression model (equation (2)):

$$\mathbf{y_{data}} = \mathbf{X_{ep}}\boldsymbol{\beta}_{\mathbf{ep}} + \boldsymbol{\varepsilon} \tag{2}$$

Where:

$\mathbf{y_{data}}$ is the temporally calibrated data series
$\mathbf{X_{ep}}$ is a matrix of sine and cosine predictor terms representing the eccentricity and precession periods
$\boldsymbol{\beta}_{\mathbf{ep}}$ is a vector of regression coefficients for each predictor
$\boldsymbol{\varepsilon}$ is a vector of error terms

In addition to the five dominant eccentricity periods that are used as predictors in equation (1), $\mathbf{X_{ep}}$ also includes the dominant precession periods. Unlike eccentricity, the precession periods are influenced by changes in Earth's rotation rate and the dynamical ellipticity of the planet; tidal-friction results in shorter periods in the past [*Berger et al*., 1992; *Laskar et al*., 2004; *Waltham*, 2015]. Following specification of the predicted precession periods (e.g., using *Laskar et al*. [2004]; Table 1], the amplitude and phase of each astronomical term is determined during the linear model optimization (the two advantages noted previously apply). The quality of the fit is assessed by calculation of the correlation between the fitted astronomical model series, $\mathbf{f}(\mathbf{X_{ep}},\boldsymbol{\beta}_{\mathbf{ep}})$, and the temporally calibrated series ($\mathbf{y_{data}}$), yielding $r^2_{spectral}$. The final measure of fit (r^2_{opt}), which combines information from the assessment of both the amplitude envelope and spectral power, is determined as:

$$r^2_{opt} = r^2_{envelope}\ r^2_{spectral} \tag{3}$$

Thus, r^2_{opt} is the product of the fraction of variance shared between "model and time-calibrated envelope" and "model and time-calibrated data". This optimization approach identifies the sedimentation rate at which the hypothesized precession envelope expresses expected eccentricity modulation, while simultaneously spectral power is concentrated at the precession (carrier) and eccentricity (modulator) frequencies. The parameter r^2_{opt} can assume values ranging from 0 to 1 (one is a perfect fit to the models) and provides a measure of the overall quality of the astronomically calibrated time series. The statistical significance of the observed r^2_{opt} is determined via Monte Carlo simulation with a first-order autoregressive model [*Gilman et al*., 1963]; other noise models may be substituted as desired to test a range of null hypotheses.

To illustrate the TimeOpt method, a 1000 ka long model with a 5 ka sampling interval (Figure 1a) is constructed using eccentricity and precession signals [*Laskar et al*., 2004] that are standardized before combining (zero mean and unit variance; these are henceforth referred to as "EP" models). The temporal series is then transformed to depth using a sedimentation rate of 2 cm/ka. Regression modeling (equations (1) and (2)) uses five eccentricity periods (405.7 ka, 130.7 ka, 123.8 ka, 98.9 ka, and 94.9 ka [*Laskar et al*., 2011a]) and four precession periods (23.6 ka, 22.3 ka, 19.1 ka, and 18.9 ka [*Laskar et al*., 2004]), and the precession amplitude envelope is extracted using a Taner filter with half-power points at 0.035 and 0.065 cycles/ka (roll-off rate of 10^3 [*Taner*, 1992]). Analysis of the record is conducted using a grid of 100 sedimentation rates spanning 1.3 to 4.95 cm/ka, which covers the entire range of sedimentation rates for which the astronomical terms can be fully evaluated, given sampling limitations (the Nyquist and Rayleigh frequencies) and filter parameters. Logarithmic scaling of the sedimentation rate grid compensates for the commonly observed feature of more rapid variability at low sedimentation rates (see also *Meyers et al*. [2012]).

The envelope regression model (equation (1)) identifies maximum $r^2_{envelope}$ (0.912; Figure 1e) at a sedimentation rate of 1.92 cm/ka. A second large local maximum occurs at 4.82 cm/ka ($r^2_{envelope} = 0.778$; Figure 1e), indicating an additional calibration where eccentricity-like amplitude modulation emerges, although little spectral power is present at the astronomical periods ($r^2_{spectral} = 0.260$). A number of smaller local $r^2_{envelope}$ maxima (<0.30) are also observed, emphasizing the potential for erroneous time scale identification when nonoptimization approaches are used to evaluate cyclostratigraphic records (as is common in cyclostratigraphy).

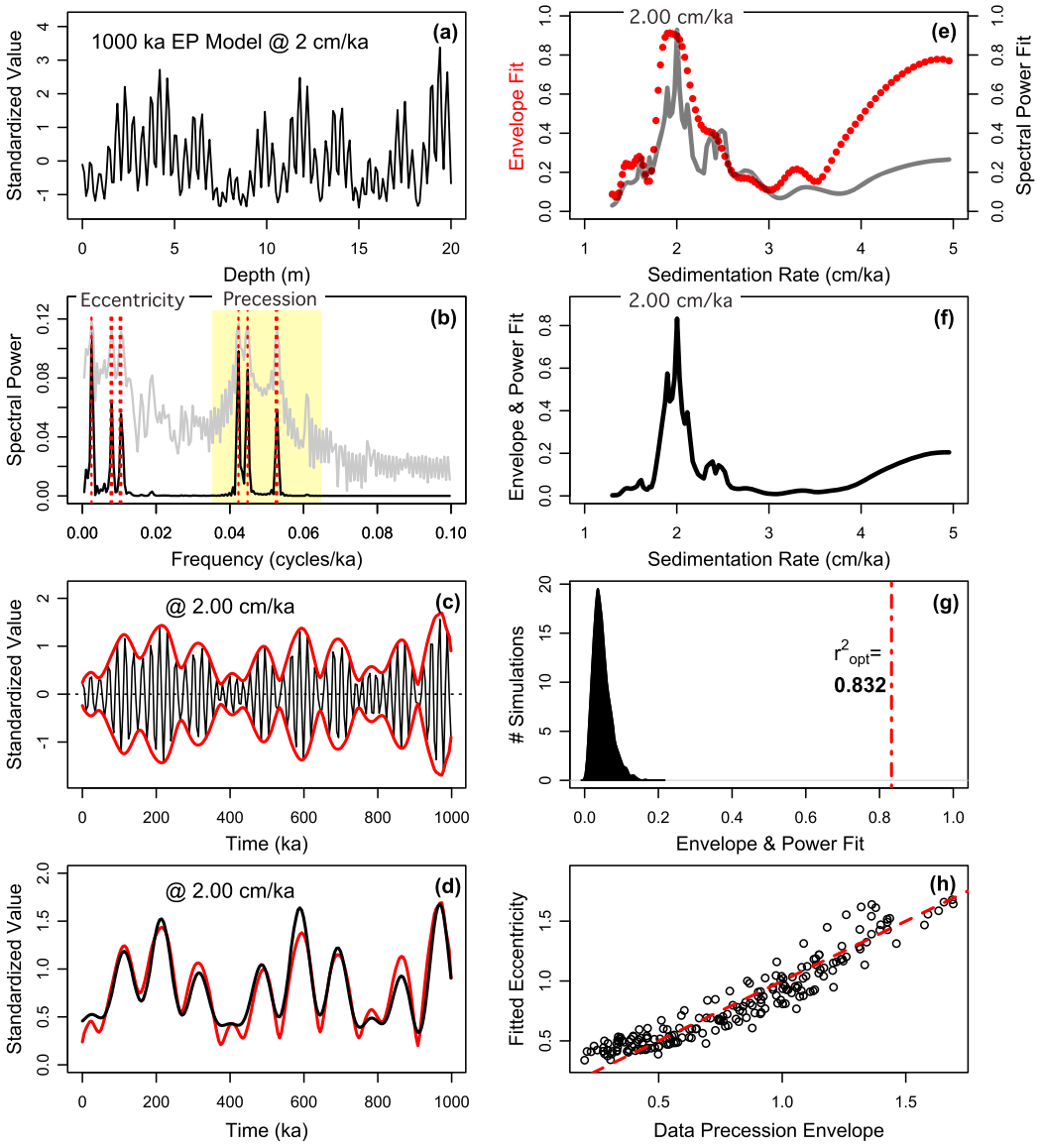

Figure 1. Demonstration of TimeOpt using a standardized eccentricity + precession (EP) model (0–1000 ka, sampling interval of 5 ka), with a sedimentation rate of 2 cm/ka. (a) The EP stratigraphic model. (b) Periodogram for the EP model, given the TimeOpt derived sedimentation rate of 2.00 cm/ka (black line = linear spectrum; gray line = log spectrum). Yellow shaded region indicates the portion of the spectrum bandpassed for evaluation of the precession amplitude envelope. Dashed red lines indicate the eccentricity and precession target periods. (c) Comparison of the band-passed precession signal (black), and the data amplitude envelope (red) determined via Hilbert transform. (d) Comparison of the data amplitude envelope (red) and the TimeOpt-reconstructed eccentricity model (black; derived using equation (1)). (e) Squared Pearson correlation coefficient for the amplitude envelope fit ($r^2_{envelope}$; red dots) and the spectral power fit ($r^2_{spectral}$; dark gray line) at each evaluated sedimentation rate. (f) Combined envelope and spectral power fit (r^2_{opt}) at each evaluated sedimentation rate. (g) Summary of 2000 Monte Carlo simulations with AR1 surrogates ($\rho_{AR1} = 0.552$), used to evaluate the significance of the maximum observed r^2_{opt} of 0.832. (h) Cross plot of the data amplitude envelope and the TimeOpt-reconstructed eccentricity model in panel "d"; dashed red line is the 1:1 line.

The spectral power regression model (equation (2)) identifies maximum $r^2_{spectral}$ (0.928; Figure 1e) at 2.00 cm/ka, as does the combined model (equation (3)), which yields a maximum r^2_{opt} of 0.832 (Figure 1f). Monte Carlo simulation with 2000 AR1 surrogates that posses the same lag-1 autocorrelation coefficient as the data ($\rho_{AR1} = 0.552$) yields a p-value of 0.005 for the observed r^2_{opt} at 2.00 cm/ka, indicating a highly significant result (Figure 1g). The excellent fit of the target periods to the observed periods using the optimal sedimentation rate of 2.00 cm/ka is illustrated in the power spectrum of Figure 1b, and the excellent fit of the time-calibrated

envelope to the TimeOpt-reconstructed eccentricity model (derived using equation (1)) is shown in Figures 1d and 1h. For comparison, analysis of an AR1 noise model using the TimeOpt approach is illustrated in Figure S1 in the supporting information, demonstrating the low statistical significance of the r^2_{opt} result (p-value = 0.398) as expected.

The *nominal* TimeOpt approach outlined above involves two fundamental assumptions, the first of which is that the eccentricity and precession periods can be reliably estimated using theoretical astronomical models. In the present study, the astronomical solutions of *Laskar et al*. [2004; "LA04"] and *Laskar et al*. [2011a; "LA10d"] are used, although other models may be substituted as desired [e.g., *Berger et al*., 1992; *Varadi et al*., 2003; *Laskar et al*., 2011b; *Waltham*, 2015]. The second fundamental assumption is that sedimentation rate is constant within the stratigraphic interval investigated, with no significant hiatus. To address this issue, changes in sedimentation rate can be evaluated using an evolutive (moving window) implementation of TimeOpt, or more simply, although the application of time-frequency analysis methods [e.g., *Prokoph and Agterberg*, 1999; *Meyers et al*., 2001; *Meyers and Sageman*, 2004] to identify stable intervals for subsequent TimeOpt assessment.

In addition to the *nominal* constant sedimentation rate model that is the focus of the present study, the statistical methodology that comprises TimeOpt can also accommodate a range of other sedimentation models. For example, the TimeOpt method can be adapted to simultaneously optimize on a best fit average sedimentation rate, and a best fit model for linearly increasing/decreasing sedimentation rates through a study interval. Similarly, one could simultaneously optimize on a best fit model for variable accumulation across hemicycles (differential accumulation). These complex models are more computationally demanding, and their execution requires a greater degree of sophistication, but the basic principles follow from the *nominal* TimeOpt approach. For reference, application of the *nominal* TimeOpt approach to EP models characterized by linear sedimentation rate increase, and differential accumulation, are included in Figures S2 and S3. It should be noted that while these nonsteady sedimentation models illustrate some degradation of r^2_{opt}, the *nominal* TimeOpt approach provides reasonable approximations of the average sedimentation rate in each case.

It is clear that the complexity of some cyclostratigraphic records will demand explicit incorporation of linear sedimentation and differential accumulation model components. Bearing this in mind, the intent of the present study is to establish and evaluate the *nominal* TimeOpt approach, providing the foundation for inclusion of more elaborate sedimentation models. It is important to stress that the *nominal* TimeOpt approach is intended to serve as an objective ("hands off") astronomical testing method to support a comprehensive (e.g., cycle by cycle) tuning; ultimately, such comprehensive tuning can more accurately reconstruct variable sedimentation rates within a study interval. For the two case studies investigated here (ODP Site 926B and ODP Site 1262) comprehensive astronomical tuning exercises have already been conducted and published [*Pälike et al*., 2006a; *Westerhold et al*., 2007], and as discussed in sections 4 and 5, these astronomical time scales are independently supported by the TimeOpt results. Through these two case studies, and a range of simulations (section 3, Supporting Information), the *nominal* approach is demonstrated to provide a valuable tool for astrochronology.

3. Statistical Power of TimeOpt

When considering the usefulness of an astrochronologic testing method for the evaluation of stratigraphic data, we must be concerned with two related issues: (1) the *significance* of the result, usually reported as a p-value, which indicates the reliability of the method in repeated use (if we use a critical p-value of 0.05, we accept that we will erroneously reject the null hypothesis of no astronomical influence 5% of the time that we apply the method), and (2) the *statistical power* of the method (note the distinction between "statistical power" and "spectral power"), which is a measure of the ability of the method to correctly detect that the null hypothesis is false when an astronomical signal is indeed present. Statistical power is reported as a probability (0–100%), with low values indicating that the method is not very sensitive, in which case it will generally fail to find astronomical cycles when they are present.

Ideally, an astrochronologic testing technique should have high statistical power, although statistical power has rarely been evaluated in astrochronologic studies (however, see *Huybers and Wunsch* [2005] and *Meyers* [2012]). The statistical power of TimeOpt is expected to be dependent upon the "shape" of the noise (AR1 coefficient, ρ_{AR1}) and its strength relative to the astronomical signals under investigation. Here we evaluate

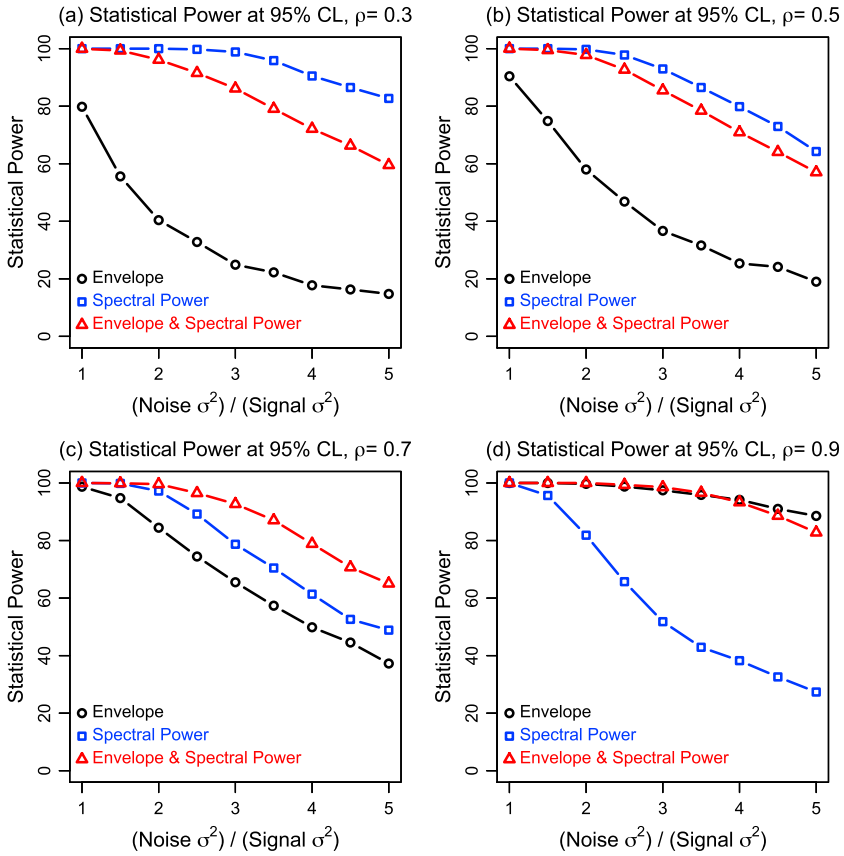

Figure 2. Assessment of statistical power for the detection of astronomical cycles at the 95% confidence level, for a sedimentation rate of 2 cm/ka, using the amplitude envelope fit ($r^2_{envelope}$ associated with equation (1); black circles), spectral power fit ($r^2_{spectral}$ associated with equation (2); blue squares) and combined fit (r^2_{opt} of equation (3); red triangles). The assessment uses 2000 AR1 simulations, with varying noise variance to signal variance ratios ($\sigma^2_{noise}/\sigma^2_{signal}$) from 1 to 5, and four different ρ_{AR1} values. The astronomical signal is a standardized eccentricity + precession (EP) model (as in Figure 1). (a) Simulations using ρ_{AR1} of 0.3, representing a weakly red process. (b) Simulations using ρ_{AR1} of 0.5, representing a moderately red process. (c) Simulations using ρ_{AR1} of 0.7, representing a strongly red process. (d) Simulations using ρ_{AR1} of 0.9, representing a very strongly red process.

the statistical power of the TimeOpt method at the 95% confidence level (p-value = 0.05), using a range of noise variance to signal variance ratios ($\sigma^2_{noise}/\sigma^2_{signal}$) from 1 to 5, and four different ρ_{AR1} values representing weakly red ($\rho_{AR1} = 0.3$; Figure 2a), moderately red ($\rho_{AR1} = 0.5$; Figure 2b) strongly red ($\rho_{AR1} = 0.7$; Figure 2c) and very strongly red ($\rho_{AR1} = 0.9$; Figure 2d) noise. In each simulation, the noise is added to a normalized EP model (as in Figure 1) to evaluate statistical power. The TimeOpt analysis parameters utilized are identical to those employed in the model analysis of Figure 1. For each of the four modeled ρ_{AR1} values, 2000 AR 1 simulations are evaluated at nine values of $\sigma^2_{noise}/\sigma^2_{signal}$. The statistical power reported in Figure 2 represents the percentage of the 2000 simulations that correctly reject the null hypothesis (p-value ≤ 0.05) at a sedimentation rate of 2 cm/ka,

As expected, the statistical power of the method degrades as $\sigma^2_{noise}/\sigma^2_{signal}$ increases (red lines in Figure 2). Given equal noise and signal variance, astronomical cycles are identified in all simulations (100%) using r^2_{opt}, but this decreases to values as low as 57% when $\sigma^2_{noise}/\sigma^2_{signal}$ is 5 (Figure 2b). For comparison, statistical power associated with the amplitude envelope fit ($r^2_{envelope}$, black lines; equation (1)) and the spectral power fit ($r^2_{spectral}$, blue lines; equation (2)) are also displayed. In the case of the weakly red simulations ($\rho_{AR1} = 0.3$; Figure 2a), the spectral power fit ($r^2_{spectral}$) consistently yields higher statistical power than the combined fit (r^2_{opt}), while the amplitude envelope fit ($r^2_{envelope}$) consistently displays the lowest statistical power. This contrasts with the very strongly red simulations ($\rho_{AR1} = 0.9$; Figure 2d); in this case the spectral power fit ($r^2_{spectral}$) is characterized by the lowest statistical power, while the amplitude envelope fit ($r^2_{envelope}$) and combined fit

(r^2_{opt}) are similar. Simulations using ρ_{AR1} of 0.5 (Figure 2b) and 0.7 (Figure 2c) illustrate the transition between these two extremes.

The ρ_{AR1}-dependent statistical power trends illustrated in Figure 2 are a consequence of changes in the noise spectrum power distribution, and resultant interference between the noise and astronomical signal. When ρ_{AR1} is small, variance is more evenly distributed across the power spectrum, allowing strong precession and eccentricity signals to be almost equally-well preserved, but nonetheless adding a substantial amount of noise within the precession band (0.035–0.065 cycles/ka) that is extracted for envelope assessment (Figure 2a). As a consequence, the eccentricity-related amplitude modulation of precession is preferentially corrupted. In contrast, when ρ_{AR1} is large there is a concentration of spectral power in the low frequencies, preferentially corrupting the eccentricity cycles, while less noise is contributed to the precession band used for envelope assessment (Figure 2d). In sum, if the data spectrum is too red, then the amplitude envelope of precession has a better performance, while if the spectrum is too white, direct assessment of the eccentricity and precession spectral power demonstrates better performance; in either case r^2_{opt} generally performs well. Based on the simulations, we can conclude that the fidelity of these two signal attributes (amplitude envelope versus spectral power) is antithetical, and strongly dependent upon the character of the noise. However, the statistical power of the combined fit (r^2_{opt}) is consistently high ($\geq$85% for $\sigma^2_{noise}/\sigma^2_{signal} \leq 3$).

4. Case Study I: The PETM-ETM2 Interval From the Walvis Ridge Transect, ODP Site 1262 (Leg 208)

ODP Leg 208 recovered late Paleogene strata from a depth transect across the Walvis Ridge and the adjacent Angola Basin (South Atlantic [*Zachos et al*., 2004]). This archive has provided an invaluable record of the late Paleocene-early Eocene hyperthermal events, including comprehensive astrochronologies for the interval [*Lourens et al*., 2005; *Westerhold et al*., 2007, 2012]. *Lourens et al*. [2005] developed astrochronologies from core material at ODP Sites 1262 and 1267 using magnetic susceptibility and L* (lightness) data. Comparison of these data sets with theoretical orbital eccentricity models [*Varadi et al*., 2003; *Laskar et al*., 2004] suggested that two of the early Eocene hyperthermal events, the PETM (Paleocene-Eocene Thermal Maximum) and ETM2 (Eocene Thermal Maximum 2, or "ELMO"), were paced by similar orbital configurations. According to this interpretation, the two events occur during maxima in both the ~100 ka and 405 ka eccentricity cycles, following prolonged minima in the longer period ~2250 ka eccentricity cycle. Subsequent cyclostratigraphic analysis by *Westerhold et al*. [2007] used X-ray fluorescence (XRF) iron data and a* color reflectance data (red/green ratio) from multiple sites at Walvis Ridge (and ODP Site 1051; Blake Nose), in conjunction with improved spliced composite depth scales, to refine and extend the astrochronology. Their results supported the occurrence of the PETM and ETM2 during maxima in ~100 ka eccentricity, but suggested more complex relationships with the longer period eccentricity cycles. *Westerhold et al*. [2012] further evaluated XRF iron data from ODP Sites 1258 and 1262 against updated astronomical solutions [*Laskar et al*., 2011a, 2011b] to develop an astronomically calibrated time scale for the interval from 47 to 65 Ma.

Here we investigate the a* (red/green ratio) color reflectance data from ODP Site 1262, which is the deepest of the Leg 208 sites [*Zachos et al*., 2004]. As in *Lourens et al*. [2005], we focus on the interval between the PETM and ETM2, spanning ~22.4 m. The sediments generally consist of nannofossil ooze with some chert layers. In contrast, the PETM and ETM2 events are expressed as deep-red clay layers. *Westerhold et al*. [2007] demonstrate that the a* data through this interval have a strong positive correlation with iron XRF counts, and increases in both of these parameters are interpreted to reflect greater terrigenous content. Prior to evaluation with TimeOpt, the a* data is interpolated to an even sampling grid, and a linear trend is removed (it is recommended to interpolate on a grid that is equal to or greater than the median sampling interval, and in this case the median sampling interval of 0.02 m is used). Analysis of the record is conducted using the precession and eccentricity targets outlined in Table 1 (derived from spectral analysis of the solutions of *Laskar et al*. [2004, 2011a]), a precession filter band of 0.035–0.065 cycles/ka (half-power points; roll-off rate of 10^3), and a grid of 100 sedimentation rates spanning 0.5 to 3 cm/ka. These sedimentation rates encompass values that are consistent with prior average background estimates based on astrochronology, magnetostratigraphy, and biostratigraphy (see discussion below [*Röhl et al*., 2003; *Zachos et al*., 2004; *Lourens et al*., 2005; *Westerhold et al*., 2007]).

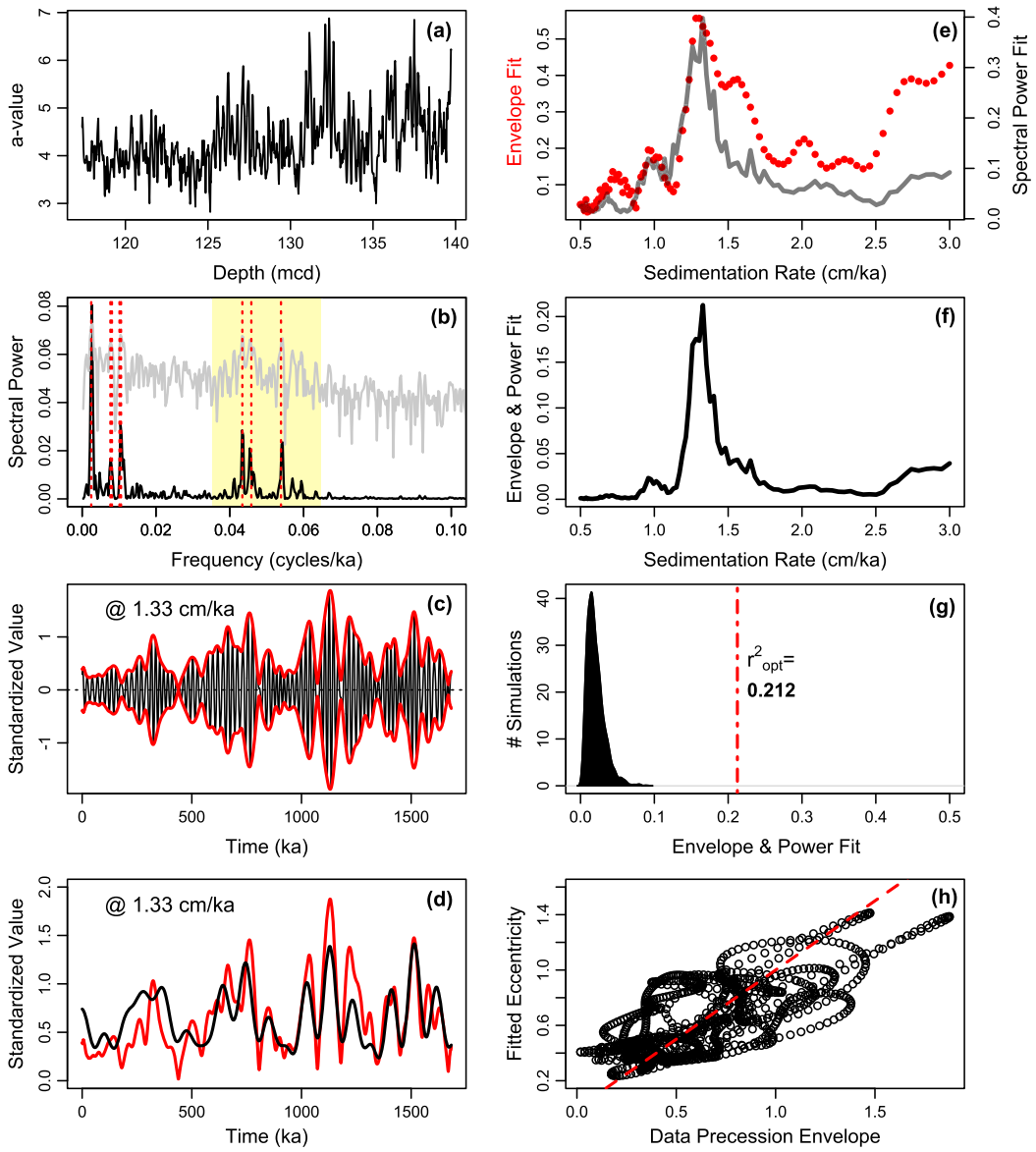

Figure 3. TimeOpt analysis of color data (a*, representing the red/green ratio) from ODP Site 1262, spanning the interval between the PETM and ETM2. (a) The 1262 color data. (b) Periodogram for the Site 1262 color data, given the TimeOpt derived sedimentation rate of 1.33 cm/ka (black line = linear spectrum; gray line = log spectrum). Yellow shaded region indicates the portion of the spectrum bandpassed for evaluation of the precession amplitude envelope. Dashed red lines indicate the eccentricity and precession target periods. (c) Comparison of the band-passed precession signal (black), and the data amplitude envelope (red) determined via Hilbert transform. (d) Comparison of the data amplitude envelope (red) and the TimeOpt-reconstructed eccentricity model (black; derived using equation (1)). (e) Squared Pearson correlation coefficient for the amplitude envelope fit ($r^2_{envelope}$; red dots) and the spectral power fit ($r^2_{spectral}$; dark gray line) at each evaluated sedimentation rate. (f) Combined envelope and spectral power fit (r^2_{opt}) at each evaluated sedimentation rate. (g) Summary of 2000 Monte Carlo simulations with AR1 surrogates ($\rho_{AR1} = 0.907$), used to evaluate the significance of the maximum observed r^2_{opt} of 0.212. (h) Cross plot of the data amplitude envelope and the TimeOpt-reconstructed eccentricity model in panel "d"; dashed red line is the 1:1 line.

The envelope regression model (equation (1)) identifies maximum $r^2_{envelope}$ at a sedimentation rate of 1.28 cm/ka (0.557; Figure 3e). The spectral power regression model (equation (2)) identifies maximum $r^2_{spectral}$ at 1.33 cm/ka (0.398; Figure 3e), as does the combined model (equation (3)), which results in a maximum r^2_{opt} of 0.212 (Figure 3f). Monte Carlo simulation using 2000 AR1 surrogates with the same lag-1 autocorrelation coefficient as the data ($\rho_{AR1} = 0.907$) yields a *p*-value of 0.005 for the maximum observed r^2_{opt} at 1.33 cm/ka, indicating that we can reject the null hypothesis at the 99.5% confidence level (Figure 3g). The fit of the target periods to the observed periods

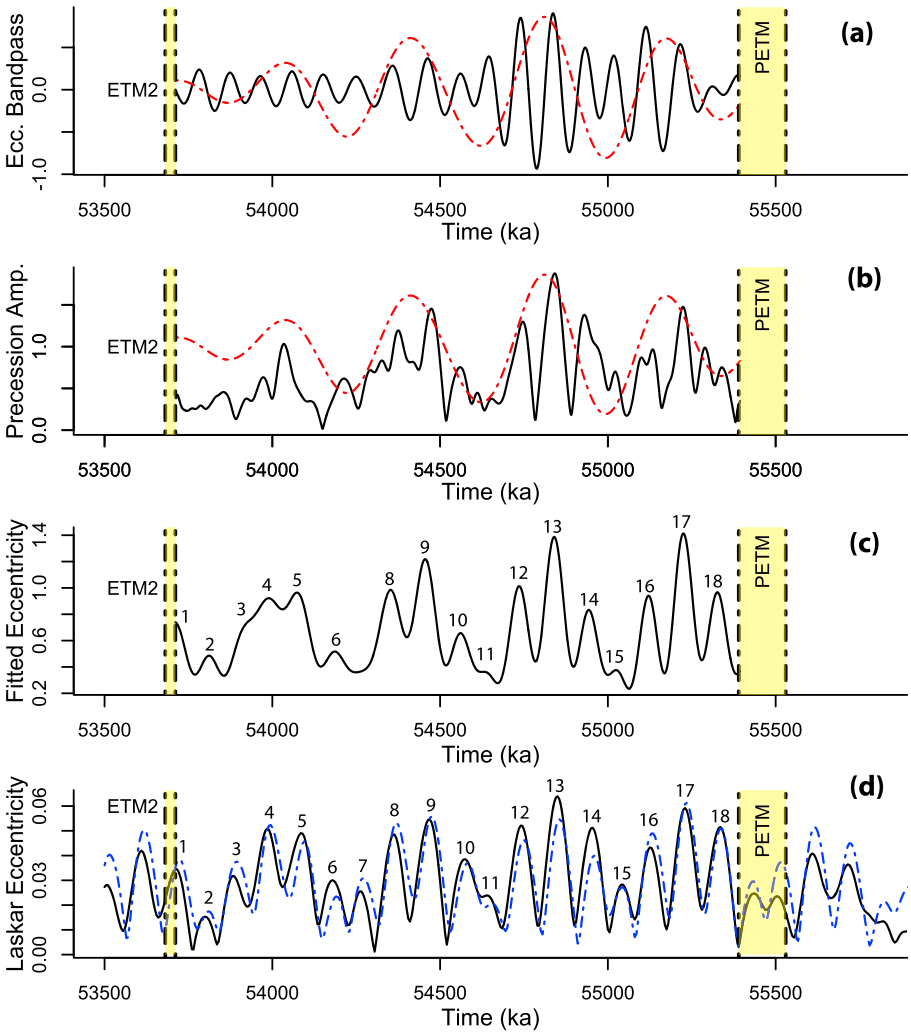

Figure 4. Examination of the observed eccentricity-scale a* cycles at ODP Site 1262. The floating astrochronology is anchored at the ETM2 (option 1 of *Westerhold et al.* [2007]) and uses a constant sedimentation rate derived from the TimeOpt analysis (1.33 cm/ka). (a) Eccentricity filter outputs (black line = short eccentricity; red dashed line = long eccentricity) from the tuned a* time series. Long eccentricity was extracted using a Taner filter with half power points at 1/650 ka and 1/250 ka, and a roll-off rate of 10^4. Short eccentricity was extracted using a Taner filter with half power points at 1/140 ka to 1/80 ka and a roll-off rate of 10^4. (b) The observed precession envelope (black line) and the long-eccentricity band-pass filter output from the tuned a* time series (red dashed line). (c) The TimeOpt-reconstructed eccentricity model (derived using equation (1)). (d) The *Laskar et al.* [2004] eccentricity solution (black line) and the *Laskar et al.* [2011a] "10d" eccentricity solution (blue dashed line). Numbers 1–18 in Figures 4c and 4d identify short eccentricity cycles. Note that the a* data was standardized prior to analysis (mean value of zero, standard deviation of unity), and thus, the ordinate of the plots in Figures 4a–4c reflects a standardized value.

using the optimal sedimentation rate of 1.33 cm/ka is illustrated in the spectrum of Figure 3b, and the fit of the time-calibrated envelope to the TimeOpt-reconstructed eccentricity model is shown in Figures 3d and 3h.

The TimeOpt derived sedimentation rate of 1.33 cm/ka is similar to prior estimates based on astrochronology, magnetostratigraphy, and biostratigraphy. For example, the average sedimentation rate for Chron C24r, which is substantially broader than the interval studied here, is ~1.3 cm/ka based on the astrochronology of *Röhl et al.* [2003], and ~1.9 cm/ka based on the astrochronology of *Westerhold et al.* [2007]. Biostratigraphically derived sedimentation rates for the interval studied here are ~1.2 cm/ka [*Zachos et al.*, 2004].

Figure 4 further evaluates the preserved astronomical rhythms at ODP Site 1262 and compares the TimeOpt results to the theoretical astronomical solutions [*Laskar et al.*, 2004, 2011a]. To do so, the depth-scaled a* data are transformed to time using the TimeOpt derived sedimentation rate of 1.33 cm/ka (a constant sedimentation

rate is used, and thus, no fine-scale tuning is applied), and the resultant floating astrochronology is anchored to the ETM2 event (53.69 Ma) using "option 1" of *Westerhold et al*. [2007]; note that the locations of the PETM and ETM2 using "option 1" are highlighted in yellow in Figure 4). This analysis indicates that the total amount of time between the end of the PETM and the start of ETM2, as derived from the floating TimeOpt time scale (~1680 ka), is in close agreement with that of *Westerhold et al*. [2007].

There are several lines of evidence that speak to the remarkable fidelity of the preserved record of eccentricity at ODP Site 1262. First, the long and short eccentricity signals, as extracted using band-pass filtering (see Figure 4 caption for filter parameters), demonstrate the expected coherence between the amplitude modulation of short eccentricity, and the preserved long eccentricity signal (Figure 4a). Coherence with the filtered long eccentricity signal is also expressed in the amplitude modulation of precession (Figure 4b), and in the TimeOpt-reconstructed eccentricity model (Figure 4c; derived using equation (1)). None of these relationships with the filtered long eccentricity signal at Site1262 (red dashed line in Figures 4a and 4b) are predefined by the TimeOpt analysis; that is, they are emergent properties that further support the validity of the derived time scale.

In addition, the TimeOpt-calibrated cycles show good agreement with the theoretical eccentricity models of *Laskar et al*. [2004, 2011a]. Strikingly, the TimeOpt-reconstructed eccentricity model (Figure 4c) displays 17 of the 18 predicted short eccentricity cycles, and it closely reproduces the detailed amplitude structure observed in the *Laskar et al*. [2004, 2011a] solutions, even though a simple constant sedimentation rate model is used. However, the assumption of a constant sedimentation rate likely contributes some of the observed discrepancies as well (such as the absence of cycle "7"; Figure 4c), and time-frequency analysis (Figure S4) reveals some sedimentation rate variability within the study interval.

A phase offset between the maxima of the reconstructed eccentricity model and the theoretical solutions is also present (Figures 4c and 4d). For the 15 well-resolved peaks (excluding cycles 1, 3, and 7), the phase offset for LA10d ranges from 5 to 31 ka, and the offset for LA04 ranges from −6 to 24 ka, indicating that the Laskar solutions typically predict older maxima than the Site 1262 eccentricity model. This phase shift could be due to several factors: (1) changes in sedimentation rate within the study interval (see Figure S4), (2) anchoring of the TimeOpt result (the numerical age assigned to the onset of ETM2), (3) insolation-climate-deposition transfer functions that distort the phase of the precession envelope used in the model fit (equation (1)) [e.g., *Laurin et al*., 2005], and/or (4) inaccuracies in the LA04/LA10d theoretical models. However, more generally speaking, we can conclude that the TimeOpt results from ODP Site 1262 provide a strong independent confirmation of the veracity of the astronomical solutions and support the astrochronology of *Westerhold et al*. [2007]. In particular, the detailed match between the TimeOpt-reconstructed eccentricity model (Figure 4c) and the *Laskar et al*. [2004, 2011a] solutions independently supports PETM tuning option 1 of *Westerhold et al*. [2007, 2012], with a mismatch of no more than 31 ka.

5. Case Study II: Miocene Strata From Ceara Rise, ODP Site 926B (Leg 154)

Cyclostratigraphic analysis of Oligocene and Miocene strata from the equatorial Atlantic Ceara Rise has played an essential role in the development of the geologic time scale, the validation of the theoretical astronomical solutions, and in evaluating the history of the Antarctic ice sheets [*Weedon et al*., 1997; *Zachos et al*., 1997; *Shackleton et al*., 1999; *Pälike et al*., 2006a, 2006b]. Here we examine benthic foraminifera $\delta^{18}O$ data spanning 440–490 m composite depth from Site 926B [*Pälike et al*., 2006a], which has been previously investigated using the average spectral misfit (ASM) method for astrochronologic testing [*Meyers*, 2012]. Prior to evaluation with TimeOpt, the $\delta^{18}O_{benthic}$ data from this interval are interpolated to a sample spacing of 0.1 m (81% of the study interval has a sample spacing ≤ 0.1 m), and a long-term trend is removed using a lowess smoother (frequencies <0.06 cycles/m [*Cleveland*, 1979]). Analysis of the record is conducted using the precession and eccentricity targets outlined in Table 1, a precession filter band of 0.035–0.065 cycles/ka (half-power points; roll-off rate of 10^3), and a grid of 100 sedimentation rates spanning 1.3 to 5 cm/ka. These sedimentation rates encompass values that are consistent with prior average background estimates based on biostratigraphy [*Weedon et al*., 1997] and cyclostratigraphy [*Weedon et al*., 1997; *Pälike et al*., 2006a]; the lowermost value of 1.3 cm/ka is also the smallest permitted for TimeOpt analysis, given the Nyquist frequency and filter parameters.

The spectral power regression model (equation (2)) identifies maximum $r^2_{spectral}$ (0.300; Figure 5e) at 2.94 cm/ka. The envelope regression model (equation (1)) identifies maximum $r^2_{envelope}$ (0.371; Figure 5e) at a sedimentation

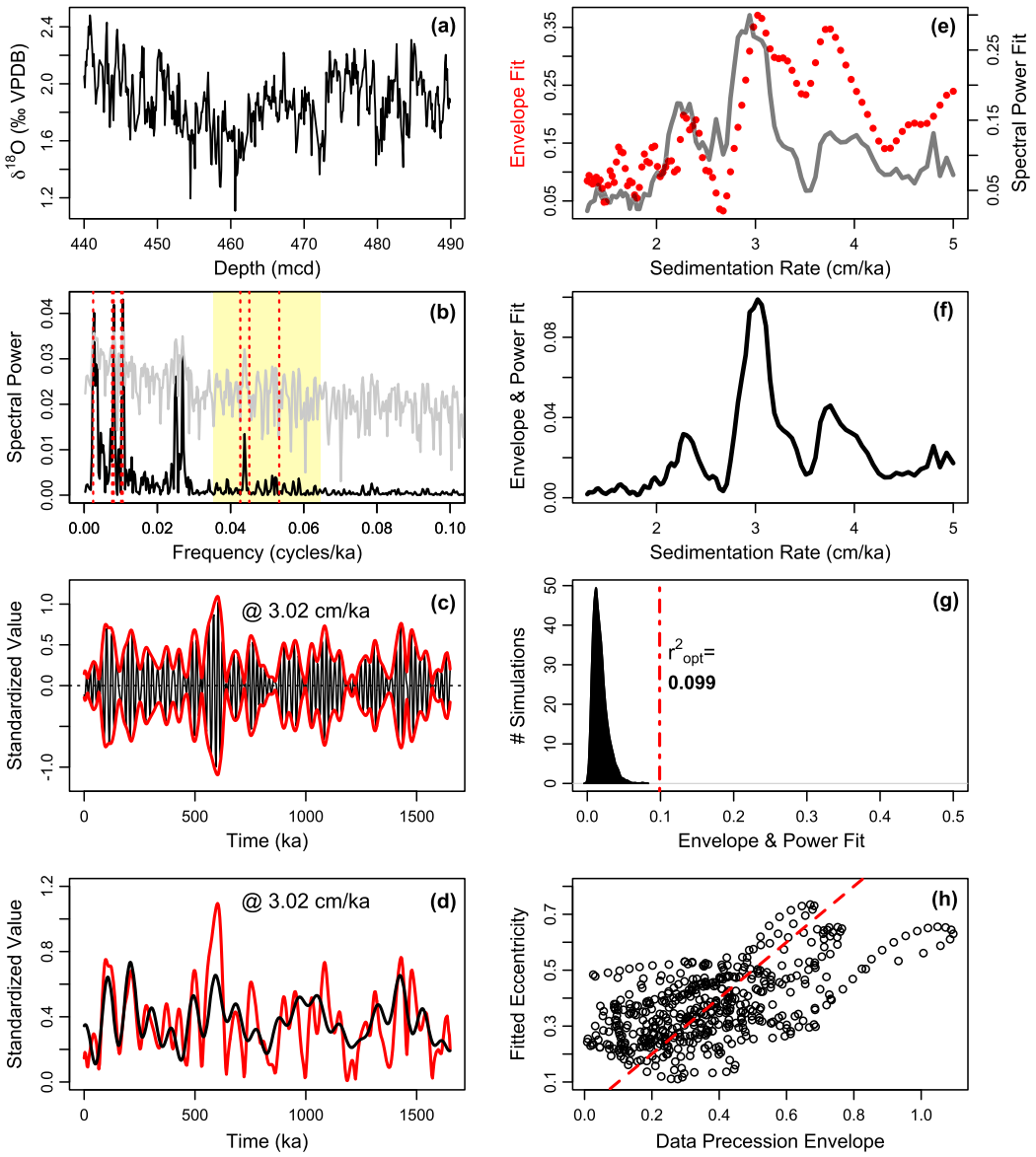

Figure 5. TimeOpt analysis of Miocene benthic foraminifera $\delta^{18}O$ data (440–490 m composite depth) from ODP Site 926B on the Ceara Rise [*Pälike et al.*, 2006a]. (a) Benthic foraminifera $\delta^{18}O$ data (permil VPDB), adjusted for seawater disequilibrium [*Pälike et al.*, 2006a]. (b) Periodogram for the 926B $\delta^{18}O$ data, given the TimeOpt derived sedimentation rate of 3.02 cm/ka (black line = linear spectrum; gray line = log spectrum). Yellow shaded region indicates the portion of the spectrum bandpassed for evaluation of the precession amplitude envelope. Dashed red lines indicate the eccentricity and precession target periods. (c) Comparison of the band-passed precession signal (black), and the data amplitude envelope (red) determined via Hilbert transform. (d) Comparison of the data amplitude envelope (red) and the TimeOpt-reconstructed eccentricity model (black; derived using equation (1)). (e) Squared Pearson correlation coefficient for the modulation fit ($r^2_{envelope}$; red dots) and the spectral power fit ($r^2_{spectral}$; dark gray line) at each evaluated sedimentation rate. (f) Combined envelope and spectral power fit (r^2_{opt}) at each evaluated sedimentation rate. (g) Summary of 2000 Monte Carlo simulations with AR1 surrogates ($\rho = 0.706$), used to evaluate the significance of the maximum observed r^2_{opt} of 0.099. (h) Cross plot of the data amplitude envelope and the TimeOpt-reconstructed eccentricity model in Figure 6d; dashed red line is the 1:1 line.

rate of 3.02 cm/ka, as does the combined model (equation (3)), which results in a maximum r^2_{opt} of 0.099 (Figure 5f). Monte Carlo simulation using 2000 AR1 surrogates with the same lag-1 autocorrelation coefficient as the data ($\rho_{AR1} = 0.706$) yields a p-value of 0.005 for the maximum observed r^2_{opt} at 3.02 cm/ka, indicating that we can reject the null hypothesis at the 99.5% confidence level (Figure 5g). The fit of the target periods to the observed periods using the optimal sedimentation rate of 3.02 cm/ka is illustrated in the spectrum of

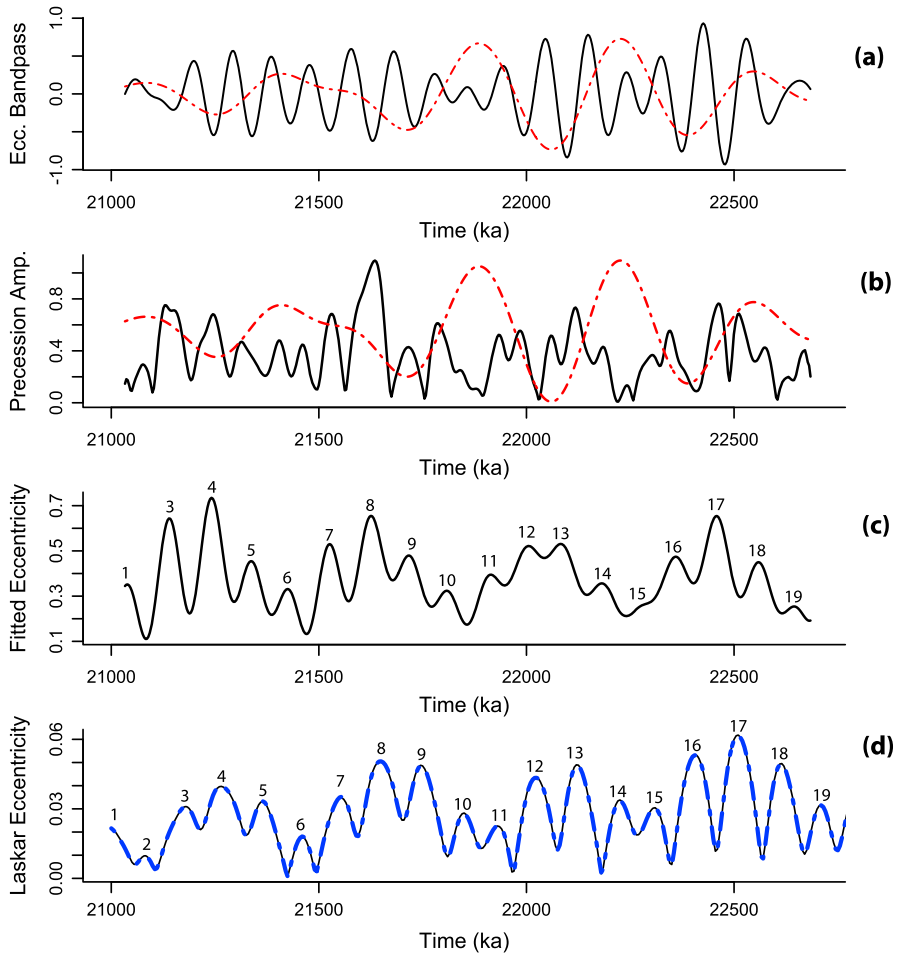

Figure 6. Examination of the observed eccentricity-scale $\delta^{18}O_{benthic}$ cycles at ODP Site 926B. The floating astrochronology is anchored to the astronomically tuned age of 21.033 Ma from *Pälike et al.* [2006a] and uses a constant sedimentation rate derived from the TimeOpt analysis (3.02 cm/ka). (a) Eccentricity filter outputs (black = short eccentricity; red = long eccentricity) from the tuned $\delta^{18}O_{benthic}$ time series. Filter parameters are identical to those used in Figure 4. (b) The observed precession envelope (black) and the long-eccentricity band-pass filter output from the tuned $\delta^{18}O_{benthic}$ time series (red). (c) The TimeOpt-reconstructed eccentricity model (derived using equation (1)). (d) The *Laskar et al.* [2004] eccentricity solution (black line) and *Laskar et al.* [2011a] "10d" eccentricity solution (blue dashed line). Numbers 1-19 in Figures 6c and 6d identify short eccentricity cycles. Note that the $\delta^{18}O_{benthic}$ data were standardized prior to analysis (mean value of zero, standard deviation of unity), and thus, the ordinate of the plots in Figures 6a–6c reflects a standardized value.

Figure 5b, and the fit of the time-calibrated envelope to the TimeOpt-reconstructed eccentricity model is shown in Figures 5d and 5h.

It is notable that a strong obliquity signal is also resolved in the power spectrum of the Site 926B $\delta^{18}O$ data (Figure 5b). This observation provides additional independent support for the TimeOpt result, as obliquity was not included in the regression models (equations (1) and (2)). Nonetheless, the presence of the $\delta^{18}O$ obliquity signal serves to reduce $r^2_{spectral}$ and r^2_{opt}. If the dominant obliquity term (40.16 ka; from spectral analysis of the *Laskar et al.* [2004] solution) is included in the spectral power regression model (equation (2)), the fit improves ($r^2_{opt} = 0.119$; Figure S5). However, the existence of a doublet (rather than a single strong obliquity peak) is unexpected, and suggests the existence of one or more unresolved hiatuses [*Meyers et al.*, 2001; *Meyers and Sageman*, 2004]. Application of the hiatus detection method of *Meyers and Sageman* [2004] indicates the presence of two temporal gaps in the study interval, each with an estimated duration of ~20 ka (Figure S6). Finally, the overall lower r^2_{opt} of the ODP Site 926B data compared to the ODP Site 1262 data (0.119 versus 0.212) reflects a generally noisier signal at Ceara Rise, due to hiatus, and perhaps other contributing factors (related to the site and/or proxy).

The TimeOpt derived sedimentation rate of 3.02 cm/ka at Site 926B compares to a prior estimate of ~2.3 cm/ka based on biostratigraphy [*Weedon et al*., 1997], 2.67-3.07 cm/ka based on spectral analysis of magnetic susceptibility data [*Weedon et al*., 1997], and an estimate of 2.95 cm/ka based on application of the average spectral misfit (ASM) astrochronologic testing method to the same benthic $\delta^{18}O$ data evaluated here [*Meyers*, 2012]. The ASM result is nearly identical to the $r^2_{spectral}$ result of 2.94 cm/ka, which is not surprising considering that both approaches evaluate the frequency arrangement (ratios) of power spectrum peaks. Additional information provided by the amplitude envelope assessment serves to slightly increase the r^2_{opt}-derived sedimentation rate. Given the small discrepancy of the results from these two methods, the optimal sedimentation rates from TimeOpt and ASM yield identical astronomical interpretations.

Figure 6 further evaluates the preserved astronomical rhythms at Site 926B and compares the TimeOpt results to theoretical astronomical solutions [*Laskar et al*., 2004, 2011a]. The depth-scaled $\delta^{18}O_{benthic}$ data are transformed to time using the TimeOpt derived sedimentation rate of 3.02 cm/ka (no fine-scale tuning is applied). The resultant floating astrochronology is anchored to the astronomically tuned age of 21.033 Ma *Pälike et al*. [2006a] at the top of the interval (440.01 m).

The TimeOpt-reconstructed eccentricity model (Figure 6c) shows good agreement with the theoretical eccentricity models of *Laskar et al*. [2004, 2011a]; Figure 6d). Eighteen of the 19 predicted eccentricity cycles are resolved, and the amplitude pattern observed in the *Laskar et al*. [2004, 2011a] solutions is reproduced in the reconstructed eccentricity model. As was the case in the Site 1262 analysis, some of the observed discrepancies are likely attributable to the assumption of a constant sedimentation rate throughout the interval, especially given the evidence for hiatus noted above (Figure S6). The phase offset between the maxima of the Site 926B eccentricity model (Figure 6c) and the theoretical solutions (Figure 6d) ranges from 15 to 66 ka, for the 16 well-resolved peaks (excluding cycles 1, 2, and 15). The greatest discrepancy occurs in the oldest portion of the record, farthest from the anchor point at 21.033 Ma, consistent with the buildup of temporal offsets due to hiatus (Figure S6).

In contrast to the Site 1262 analysis, the long eccentricity signal at Site 926B (Figure 6a) is nearly antiphased with the amplitude modulation of the observed short eccentricity signal (Figure 6a), as well as with the TimeOpt-reconstructed eccentricity model (Figure 6c). This relationship indicates a more complex climate response at the long eccentricity period, while the amplitude envelope of precession is consistent with a direct in-phase link to orbital eccentricity changes. One possible mechanism that is compatible with these observations invokes maximum precession scale ice sheet growth during extremely cold winters (high eccentricity), while a nonlinear process generates a 405 ka long eccentricity scale ice sheet response that is most sensitive to cool summers (increased ice accumulation during low eccentricity). A nonlinear response to orbital-insolation is required to generate strong eccentricity cycles in the paleoclimate archive [*Imbrie et al*., 1993], and the carbon cycle is one plausible source [*Paillard and Parrenin*, 2004]. Strong 405 ka variance has been previously documented in $\delta^{13}C_{benthic}$ data from this time interval [*Pälike et al*., 2006a, 2006b], which is strongly coherent and nearly in phase with $\delta^{18}O_{benthic}$, supporting this hypothesis. Interestingly, the short eccentricity signal at Site 926B (Figure 6a) preserves a strong ~405 ka amplitude modulation that is nearly in phase with the TimeOpt-reconstructed eccentricity model (Figure 6c) and the theoretical solutions (Figure 6d), providing additional independent support for the TimeOpt result.

6. Conclusions

Astrochronologic analysis has played a central role in the evaluation of paleoclimate change and in the development of the geologic time scale. This study presents a new approach for astrochronologic testing and time scale optimization, using the framework of probabilistic linear regression modeling. A key feature of this approach is the simultaneous evaluation of both eccentricity-related amplitude modulation of precession cycles, and spectral power "bundling" (frequency ratios) in paleoclimate data, providing a powerful approach that is resilient to common problems in cyclostratigraphic analysis (e.g., poor time control, circular reasoning, low statistical power of methods, inappropriate power spectrum confidence levels, multiple testing). The present study focuses on the evaluation of records with relatively strong precession and eccentricity signals, but it is simple to adapt the approach to evaluate the expected long-eccentricity (405 ka) modulation of short eccentricity amplitude, and also the long-period amplitude modulation of obliquity. The nominal approach introduced in this study applies a constant sedimentation rate model, but the new regression-based method

is flexible and extensible to accommodate a range of other sedimentation models (linear sedimentation rate changes, differential accumulation, etc.).

Application of the technique to cyclostratigraphic data sets from the Miocene (ODP Site 926B) and Eocene (ODP Site 1262) confirms published astronomical interpretations at the 99.5% confidence level [*Pälike et al.*, 2006a; *Westerhold et al.*, 2007] and provides support for the theoretical astronomical solutions [*Laskar et al.*, 2004, 2011a]. The TimeOpt method is relatively uncomplicated to use, and it is suitable for the evaluation of cyclostratigraphic records throughout the Phanerozoic (potentially beyond). To facilitate application of the TimeOpt method to cyclostratigraphic data sets, an R function [*R Core Team*, 2015] has been developed, which is included in the free software "Astrochron" [*Meyers*, 2014].

Acknowledgments

I would like to thank John Hartigan (Yale University) and Jay Emerson (Yale University) for their advice on the use of linear model optimization for astrochronologic testing. I also thank Linda Hinnov (George Mason University), Alberto Manlinverno (Lamont-Doherty Earth Observatory), and Graham Weedon (Met Office) for their insightful comments that improved this manuscript. This study and the Astrochron software are supported by NSF award EAR-1151438. The supporting information includes a number of supplementary figures, and Astrochon R-scripts to generate the results from ODP Sites 1262 and 926B (Figures 3 and 5). The data sets analyzed in this manuscript have been published in prior studies and can be accessed using the function "getData," which is a component of the Astrochron software (https://cran.r-project.org/web/packages/astrochron/index.html).

References

Aswasereelert, W., S. R. Meyers, A. R. Carroll, S. E. Peters, M. E. Smith, and K. L. Feigl (2013), Basin-scale cyclostratigraphy of the Green River Formation, Wyoming, *Geol. Soc. Am. Bull.*, *125*, 216–228.

Berger, A., M. F. Loutre, and J. Laskar (1992), Stability of the astronomical frequencies over the Earth's history for paleoclimate studies, *Science*, *255*, 560–566.

Cleveland, W. S. (1979), Locally weighted regression and smoothing scatterplots, *J. Am. Stat. Assoc.*, *74*, 829–836.

Gilman, D. L., F. J. Fuglister, and J. M. Mitchell Jr. (1963), On the power spectrum of 'Red Noise', *J. Atmos. Sci.*, *20*, 182–184.

Gradstein, F. M., J. G. Ogg, M. Schmitz, and G. Ogg (Eds.) (2012), *The Geologic Time Scale 2012*, vol. 2, Elsevier, Boston, Fla.

Hays, J. D., J. Imbrie, and N. J. Shackleton (1976), Variations in the Earth's orbit: Pacemaker of the ice ages, *Science*, *194*, 1121–1132.

Herbert, T. D. (1992), Paleomagnetic calibration of Milankovitch cyclicity in Lower Cretaceous sediments, *Earth Planet. Sci. Lett.*, *112*, 15–28.

Herbert, T. D. (1994), Reading orbital signals distorted by sedimentation: Models and examples, in *Orbital Forcing and Cyclic Sequences*, *Spec. Publ. 19 of the IAS (International Association Of Sedimentologists Series)*, edited by P. L. DeBoer and D. G. Smith, 576 pp., Wiley-Blackwell, Oxford, U. K.

Hinnov, L. A. (2000), New perspectives on orbitally forced stratigraphy, *Annu. Rev. Earth Planet. Sci.*, *28*, 419–475.

Hinnov, L. A. (2013), Cyclostratigraphy and its revolutionizing applications in the Earth and planetary sciences, *Geol. Soc. Am. Bull.*, *125*, 1703–1734.

Hinnov, L. A., and J. J. Park (1998), Detection of astronomical cycles in the stratigraphic record by frequency modulation (FM) analysis, *J. Sediment. Res.*, *68*, 524–539.

Huybers, P., and O. Aharonson (2010), Orbital tuning, eccentricity, and the frequency modulation of climatic precession, *Paleoceanography*, *25*, PA4228, doi:10.1029/2010PA001952.

Huybers, P., and C. Wunsch (2004), A depth-derived Pleistocene age model: Uncertainty estimates, sedimentation variability, and non-linear climate change, *Paleoceanography*, *19*, PA1028, doi:10.1029/2002PA000857.

Huybers, P., and C. Wunsch (2005), Obliquity pacing of the late Pleistocene glacial terminations, *Nature*, *434*, 491–494.

Imbrie, J., et al. (1993), On the structure and origin of major glaciation cycles: 2. The 100,000-year cycle, *Paleoceanography*, *7*, 701–738, doi:10.1029/92PA02253.

Kuiper, K., A. Deino, F. Hilgen, W. Krijgsman, P. Renne, and J. Wijbrans (2008), Synchronizing rock clocks of Earth history, *Science*, *320*(5875), 500, doi:10.1126/science.1154339.

Laskar, J., P. Robutel, F. Joutel, M. Gastineau, A. C. M. Correia, and B. Levard (2004), A long-term numerical solution for the insolation quantities of the Earth, *Astron. Astrophys.*, *428*, 261–285.

Laskar, J., A. Fienga, M. Gastineau, and H. Manche (2011a), La2010: A new orbital solution for the long-term motion of the Earth, *Astron. Astrophys.*, *A89*, doi:10.1051/0004-6361/201116836.

Laskar, J., M. Gastineau, J.-B. Delisle, A. Farres, and A. Fienga (2011b), Strong chaos induced by close encounters with Ceres and Vesta, *Astron. Astrophys.*, *532*, L4.

Laurin, J., S. R. Meyers, B. B. Sageman, and D. A. Waltham (2005), Phase lag in amplitude modulation of hemipelagic cycles: A new tool for recognition of relative sea level change, *Geology*, *33*, 569–572.

Lourens, L. J., A. Sluijs, D. Kroon, J. C. Zachos, E. Thomas, U. Röhl, J. Bowles, and I. Raffi (2005), Astronomical pacing of late Palaeocene to early Eocene global warming events, *Nature*, *435*, 1083–1087.

Malinverno, A., E. Erba, and T. D. Herbert (2010), Orbital tuning as an inverse problem: Chronology of the early Aptian oceanic anoxic event 1a (Selli Level) in the Cismon APTICORE, *Paleoceanography*, *25*, PA2203, doi:10.1029/2009PA0010769.

Mattinson, J. M. (2005), Zircon U–Pb chemical abrasion ("CA-TIMS") method: Combined annealing and multi-step partial dissolution analysis for improved precision and accuracy of zircon ages, *Chem. Geol.*, *220*, 47–66.

Meyers, S. R. (2012), Seeing red in cyclic stratigraphy: Spectral noise estimation for astrochronology, *Paleoceanography*, *27*, PA3228, doi:10.1029/2012PA002307.

Meyers, S. R. (2014), Astrochron: An R package for astrochronology. [Available at http://cran.r-project.org/package=astrochron.]

Meyers, S. R., and B. B. Sageman (2004), Detection, quantification, and significance of hiatuses in pelagic and hemipelagic strata, *Earth Planet. Sci. Lett.*, *224*, 55–72.

Meyers, S. R., and B. B. Sageman (2007), Quantification of deep-time orbital forcing by average spectral misfit, *Am. J. Sci.*, *307*, 773–792.

Meyers, S. R., B. Sageman, and L. Hinnov (2001), Integrated quantitative stratigraphy of the Cenomanian-Turonian Bridge Creek Limestone Member using evolutive harmonic analysis and stratigraphic modeling, *J. Sediment. Res.*, *71*, 627–643.

Meyers, S. R., B. B. Sageman, and M. Pagani (2008), Resolving Milankovitch: Consideration of signal and noise, *Am. J. Sci.*, *308*, 770–786.

Meyers, S. R., B. B. Sageman, and M. A. Arthur (2012), Obliquity forcing of organic matter accumulation during Oceanic Anoxic Event 2, *Paleoceanography*, *27*, PA3212, doi:10.1029/2012PA002286.

Muller, R. A., and G. J. MacDonald (2000), *Ice Ages and Astronomical Causes*, 318 pp., Springer, Chitchester, U. K.

Neeman, B. (1993), *Orbital tuning of Paleoclimate Records: A Reassessment, LBNL-39572*, Lawrence Berkeley Lab, Berleley, Calif.

Paillard, D., and F. Parrenin (2004), The Antarctic ice sheet and the triggering of deglaciations, *Earth Planet. Sci. Lett.*, *227*, 263–271.

Pälike, H., J. Frazier, and J. C. Zachos (2006a), Extended orbitally forced palaeoclimatic records from the equatorial Atlantic Ceara Rise, *Quat. Sci. Rev.*, *25*, 3138–3149.

Pälike, H., R. D. Norris, J. O. Herrle, P. A. Wilson, H. K. Coxall, C. H. Lear, N. J. Shackleton, A. K. Tripati, and B. S. Wade (2006b), The heartbeat of the Oligocene climate system, *Science*, *314*, 1894–1898.

Prokoph, A., and F. P. Agterberg (1999), Detection of sedimentary cyclicity and stratigraphic completeness by wavelet analysis: An application to Late Albian cyclostratigraphy of the Western Canada Sedimentary Basin, *J. Sediment. Res.*, *69*, 862–875.

R Core Team (2015), *R: A Language and Environment for Statistical Computing*, R Foundation for Statistical Computing, Vienna, Austria. [Available at http://www.R-project.org/.]

Röhl, U., R. D. Norris, and J. G. Ogg (2003), Cyclostratigraphy of upper Paleocene and lower Eocene sediments at Blake Nose Site 1051 (western North Atlantic), in *Causes and Consequences of Globally Warm Climates in the Early Paleogene*, edited by S. L. Wing et al., *Geol. Soc. Am. Spec. Pap.*, *369*, 576–589.

Schwarzacher, W. (1948), *Über die sedimentäre Rhythmik des Dachsteinkalkes von Lofer*, vol. 10–12, pp. 175–188, Geol. Bundesanstalt, Wien, Verhandl Heft 1947.

Shackleton, N., T. Hagelberg, and S. Crowhurst (1995), Evaluating the success of astronomical tuning: Pitfalls of using coherence as a criterion for assessing pre-Pleistocene timescales, *Paleoceanography*, *10*, 693–697, doi:10.1029/95PA01454.

Shackleton, N. J., S. J. Crowhurst, G. P. Weedon, and J. Laskar (1999), Astronomical calibration of Oligocene-Miocene time, *Philos. Trans. R. Soc. London, Ser. A*, *357*(1757), 1907–1929, doi:10.1098/rsta.1999.0407.

Spearman, C. (1904), The proof and measurement of association between two things, *Am. J. Psychol.*, *15*(1), 72–101.

Swenson, J. B. (2005), Fluviodeltaic response to sea level perturbations: Amplitude and timing of shoreline translation and coastal onlap, *J. Geophys. Res.*, *110*, F03007, doi:10.1029/2004JF000208.

Taner, M. T. (1992), In: Attributes revisited (Technical Report, Rock Solid Images, Inc.). [Available at http://rocksolidimages.com/pdf/attrib_revisited.htm.]

Taner, M. T., F. Koehler, and R. E. Sheriff (1979), Complex trace analysis, *Geophysics*, *44*, 1041–63.

Varadi, F., B. Bunnegar, and M. Ghil (2003), Successive refinements in long-term integrations of planetary orbits, *Astrophys. J.*, *592*, 620–630.

Vaughan, S., R. J. Bailey, and D. G. Smith (2011), Detecting cycles in stratigraphic data: Spectral analysis in the presence of red noise, *Paleoceanography*, *26*, PA4211, doi:10.1029/2011PA002195.

Waltham, D. (2015), Milankovitch period uncertainties and their impact on cyclostratigraphy, *J. Sediment. Res.*, *85*, 990–998.

Weedon, G. P., N. J. Shackleton, and P. N. Pearson (1997), The Oligocene time scale and cyclostratigraphy on the Ceara Rise, Western Equatorial Atlantic, *Proc. Ocean Drill. Program Sci. Results*, *154*, 101–114.

Westerhold, T., U. Röhl, J. Laskar, I. Raffi, J. Bowles, L. Lourens, and J. Zachos (2007), On the duration of magnetochrons C24r and C25n and the timing of early Eocene global warming events: Implications from the Ocean Drilling Program Leg 208 Walvis Ridge depth transect, *Paleoceanography*, *22*, PA2201, doi:10.1029/2006PA001322.

Westerhold, T., U. Röhl, and J. Laskar (2012), Time scale controversy: Accurate orbital calibration of the early Paleogene, *Geochem. Geophys. Geosyst.*, *13*, Q06015, doi:10.1029/2012GC004096.

Zachos, J. C., B. P. Flower, and H. Paul (1997), Orbitally paced climate oscillations across the Oligocene/Miocene boundary, *Nature*, *388*, 567–570.

Zachos, J. C., et al. (2004), *Proceedings ODP, Init. Repts.*, vol. 208, Ocean Drilling Program, College Station, Tex., doi:10.2973/odp.proc.ir.208.2004

Zeeden, C., S. R. Meyers, L. J. Lourens, and H. J. Hilgen (2015), Testing astronomically tuned age models, *Paleoceanography*, *30*, 369–383, doi:10.1002/2014PA002762.